# Advanced computational modelling of pollution dispersion in the North Sea

Nafea Lachhab[1], Mohammed Seaid[2], Mofdi El-Amrani[1], and Nabil El Moçayd[3]

[1] Laboratory of Mathematics and Applications, FSTT, Abdelmalek Essaadi University, Tangier, Morocco. `nafea.lachhab@etu.uae.ac.ma`, `mofdi.elamrani@gmail.com`

[2] Department of Engineering, University of Durham, South Road, Durham DH1 3LE, United Kingdom. `m.seaid@durham.ac.uk`

[3] College of Agriculture and Environmental Sciences, University Mohammed VI Polytechnic, Benguerir, Morocco. `nabil.elmocayd@um6p.ma`

**Abstract.** This study develops a robust three-dimensional computational model to predict the transport and dispersion of marine pollutants in the North Sea. Coastal vector datasets are first employed to generate a high-resolution computational mesh spanning 51.0°N-60.0°N and 4.5°W-13.1°E. Subsequently, sea-surface current fields at $(1/4)^\circ$ resolution, incorporating both wind-driven and geostrophic components, are assimilated to reconstruct velocity profiles throughout the full water column. A stochastic Lagrangian particle-tracking method is then introduced to simulate crude oil releases (40° API) from the Forties Oil Field (57.0°N, 1.0°E). The simulations indicate that particles travel an average distance of 500-600 km over a 30-day period. Moreover, dispersive processes account for approximately 60% of the total transport distance relative to advective contributions. Seasonal variability plays a decisive role in contaminant pathways; consequently, predicted spatial distributions differ substantially by release month, although comparable trends are observed for both surface and subsea discharge scenarios. The results further suggest that releases from the Forties Oil Field pose a limited coastal threat, with an estimated 3% probability of shoreline impact along the United Kingdom, given the predominantly eastward wind forcing.

**Keywords:** North Sea · Pollutant transport and dispersion · Stochastic Lagrangian particle tracking · Oil spill modelling · Monte Carlo analysis

## 1 Introduction

The North Sea is among the most intensively studied and economically exploited coastal regions worldwide. It hosts numerous oil and gas fields and plays a pivotal role in the European energy sector. In addition, its geographic site supports major commercial fisheries, seabird conservation areas, tourism, and dense shipping routes [8]. As offshore hydrocarbon development expanded, the construction of terminals and drilling platforms accelerated; consequently, concerns emerged

ICCS Camera Ready Version 2026
To cite this paper please use the final published version:
DOI: `10.1007/978-3-032-29924-6_3`

regarding ecological degradation and accidental contaminant release. Prior to 1984, environmental monitoring of seawater surrounding offshore installations was not mandatory, and early detection efforts were therefore limited in scope and consistency. In 1984, the UK Prevention of Oil and Pollution Act (1971) was amended to require structured monitoring programs at offshore drilling sites [7]. Nevertheless, contaminant detection remained heavily dependent on chemical techniques, many of which were still under development at the time. Meanwhile, operational discharges from drilling activities continued to generate long-term environmental pressures. In response to these challenges, hydrodynamic modelling methods began to emerge. For example, the SlikMap stochastic model, introduced in 1984 [17], sought to quantify environmental risks to coastlines and marine ecosystems in Norwegian waters. These early studies demonstrated that current-field modelling provides substantial value for environmental monitoring and risk assessment.

Subsequent advances in ocean modelling have enabled the prediction of velocity, temperature, and salinity throughout the full water column. These improvements have been driven by expanded observational datasets, enhanced computational capacity, and satellite remote sensing. For instance, the Geostrophic and Ekman Current Observatory (GEKCO) product [20], developed by the Centre for Topographic Studies of the Ocean and Hydrosphere (CTOH), employs satellite altimetry to estimate surface currents. Similarly, the Danish Meteorological Institute (DMI) operates a three-dimensional advective-dispersive ocean model that underpins an operational oil-spill forecasting service applied to both Greenlandic waters and the North Sea [13]. However, many existing hydrodynamic models remain inaccessible, computationally intensive, or costly to implement. Moreover, comparatively few studies have focused specifically on the environmental implications of oil spills within the North Sea region. Accordingly, this study presents the development of a computational approach to estimate three-dimensional current velocities in the North Sea and west of Shetland. The methodology builds upon earlier approaches reported in [17, 13]. Specifically, the objectives of this work are (i) to implement a problem-specific modelling method and employ a validated third-party software platform; (ii) to evaluate model predictions against historical datasets; and (iii) to quantify and document predictive reliability.

The remainder of this paper is structured as follows. Section 2 introduces the governing oceanographic equations together with the underlying theoretical framework. Subsequently, Section 3 describes the computational methodology adopted for simulating pollutant dispersion in the North Sea, including the numerical discretisation strategy and particle-tracking formulation. The results and their validation against observational and reanalysis datasets are then presented and discussed in Section 4. Finally, Section 5 summarises the principal findings of the study and outlines directions for future research.

ICCS Camera Ready Version 2026
To cite this paper please use the final published version:
DOI: 10.1007/978-3-032-29924-6_3

## 2 Mathematical modelling of pollution dispersion

This section presents the mathematical framework used to simulate pollutant transport in the North Sea. The formulation combines the governing equations of ocean motion with Ekman and geostrophic dynamics, a logarithmic representation of near-bottom flow, and a stochastic random-walk model for dispersive transport. In this way, both advective and turbulent-diffusive mechanisms are incorporated within a unified three-dimensional framework.

The motion of seawater is governed by the momentum equation

$$\frac{D\boldsymbol{v}}{Dt} - \nu \nabla^2 \boldsymbol{v} + \frac{1}{\rho}\nabla p = -2\varOmega \times \boldsymbol{v} + \boldsymbol{g} + \boldsymbol{F}_r, \tag{1}$$

where $\boldsymbol{v} = (u, v, w)^\top$ denotes the Cartesian velocity vector (m/s) in spatial coordinates $\boldsymbol{x} = (x, y, z)^\top$ (m), $\rho$ is the seawater density (kg/m$^3$), $\nu$ the kinematic viscosity (m$^2$/s), $p$ the pressure (Pa), $\varOmega = 7.29 \times 10^{-5}$ rad/s the Earth rotation rate, $\boldsymbol{g} = (0, 0, 9.81)^\top$ m/s$^2$ the gravitational acceleration, and $\boldsymbol{F}_r$ the wind forcing vector. Under the Boussinesq approximation, seawater may be treated as incompressible for large-scale ocean circulation [19], so that mass conservation reduces to

$$\frac{\partial u}{\partial x} + \frac{\partial v}{\partial y} + \frac{\partial w}{\partial z} = 0. \tag{2}$$

Wind forcing is a major driver of surface circulation. Assuming constant eddy viscosity, the Ekman solution for the wind-induced velocity components is written as

$$u_e + i v_e = \left|\boldsymbol{v}_e\right|_{z=0} e^{az} e^{i\left(\frac{\pi}{4} + az\right)}, \tag{3}$$

where $\boldsymbol{v}_e = (u_e, v_e, w_e)^\top$ is the wind-induced velocity (m/s) and $a$ (m$^{-1}$) is the decay constant. The Ekman boundary-layer depth $d_e$ is estimated by

$$d_e = \frac{7.6}{0.0068} \left|\boldsymbol{v}_e\right|_{z=0}, \tag{4}$$

from which $a = \frac{\pi}{d_e}$. The associated redistribution of surface waters modifies the sea-surface topography and generates horizontal pressure gradients. Neglecting acceleration in (1), the geostrophic velocity components are then given by

$$u_g = -\frac{1}{f\rho}\frac{\partial}{\partial y}\int_{-h}^{0} g(\varphi, z)\rho(z)\, dz + \frac{g}{f}\frac{\partial \eta}{\partial y}, \tag{5}$$

$$v_g = -\frac{1}{f\rho}\frac{\partial}{\partial x}\int_{-h}^{0} g(\varphi, z)\rho(z)\, dz + \frac{g}{f}\frac{\partial \eta}{\partial x}, \tag{6}$$

where $u_g$ and $v_g$ are the geostrophic velocities in the $x$ and $y$ directions (m/s), $\varphi$ is the latitude, $f = 2\varOmega \sin\varphi$ the Coriolis parameter (rad/s), $h$ the water depth (m), and $\eta$ the sea-surface elevation (m). The sub-surface contribution is approximated from geopotential anomaly differences $\varDelta\phi$ between two locations $n1$ and $n2$ separated by a distance $l$ as

$$\frac{\varDelta\phi_{n1} - \varDelta\phi_{n2}}{2\varOmega l \sin\varphi}. \tag{7}$$

ICCS Camera Ready Version 2026
To cite this paper please use the final published version:
DOI: 10.1007/978-3-032-29924-6_3

Near the seabed, bottom friction modifies the current structure. To represent this effect, the logarithmic law of the wall is adopted for the bottom boundary layer [9]:

$$\frac{\bar{u}}{u_*} = \frac{1}{\kappa} \ln\left(\frac{h}{ez_0}\right), \tag{8}$$

where $\bar{u}$ is the depth-averaged velocity (m/s), $u_*$ is the friction velocity (m/s), $\kappa = 0.4$ is the von Kármán constant, $e$ is the base of the natural logarithm, and $z_0$ is the roughness length (m).

Contaminant dispersion is represented through a stochastic random-walk formulation, in which the release is discretised into particles that undergo advective transport and turbulent spreading [14]. The particle displacement is written as

$$\boldsymbol{X}_{t+\Delta t} = \boldsymbol{X}_t + \boldsymbol{v}_t \Delta t + \sqrt{2\boldsymbol{D}\Delta t} \cdot \boldsymbol{\xi}, \tag{9}$$

where $\boldsymbol{X}_t$ and $\boldsymbol{X}_{t+\Delta t}$ denote the particle positions at times $t$ and $t+\Delta t$, respectively, $\boldsymbol{v}_t$ is the advective velocity (m/s), $\Delta t$ is the time step, $\boldsymbol{D}$ is the dispersion coefficient matrix (m$^2$/s), and $\boldsymbol{\xi}$ is a random variable with zero mean and unit variance. The second term in (9) represents advection, whereas the third term accounts for dispersive spreading. Following [11], the dispersion tensor is extended to three-dimensional flow as

$$\begin{aligned} D_{zx} = D_{xz} &= \frac{(a_l wu - a_t uw)h\sqrt{g}}{v_s C}, \\ D_{zy} = D_{yz} &= \frac{(a_l wv - a_t vw)h\sqrt{g}}{v_s C}, \\ D_{zz} &= \frac{(a_l w^2 + a_t uv)h\sqrt{g}}{v_s C}, \end{aligned} \tag{10}$$

where $a_l$ and $a_t$ are the longitudinal and turbulent dispersivities, set to 5.93 and 0.23, respectively; $C$ is the Chezy bed roughness coefficient ($70\,\mathrm{m}^{1/2}/\mathrm{s}$) [6], and $v_s$ is the depth-averaged flow speed.

When the transported particles represent oil droplets, vertical buoyant rise is incorporated through the terminal velocity

$$w_t = \sqrt{\frac{2gV_p(\rho_p - \rho)}{c_d \rho a_p}}, \tag{11}$$

where $\rho_p$ is the particle density, $V_p$ is the particle volume, $a_p$ is the particle projected area, and $c_d$ is the drag coefficient, taken as 0.47 for a spherical droplet. This term allows the model to account for the combined effects of advection, turbulent dispersion, and buoyancy-driven vertical motion in the transport of marine pollutants.

## 3 Computational method for pollution dispersion

In our simulations, the computational domain over the North Sea extends from 51.0°N to 60.0°N in latitude and from 4.5°W to 13.1°E in longitude. This spatial

ICCS Camera Ready Version 2026
To cite this paper please use the final published version:
DOI: 10.1007/978-3-032-29924-6_3

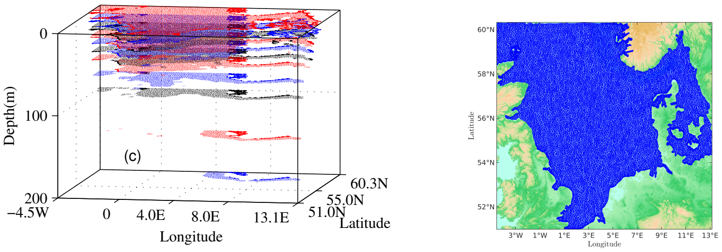

**Fig. 1.** Illustration of the computational meshes employed in the present study: the left plot displays the vertically structured meshes corresponding to the 14 discrete depth layers, whereas the right plot shows the sea-surface mesh used in the present study to resolve flow dynamics and particle transport.

configuration encompasses the principal dynamical features of the basin, including shallow coastal regions, deeper central areas, and the complex bathymetric gradients that strongly influence the circulation patterns. For the numerical simulation of the governing flow equations, we adopt a multi-layer approach for the vertical discretization [16]. In this framework, the three-dimensional system (1)-(2) is decomposed into a sequence of coupled two-dimensional problems defined on horizontal layers. Each layer is then solved using a semi-Lagrangian finite element method [10], which ensures numerical stability under relatively large time steps while retaining high accuracy in the advection-dominated regime. Consequently, the method provides an efficient and robust strategy for resolving stratified flows in shelf-sea environments. The vertical structure is represented by 14 discrete layers along the $z$-direction. These layers are defined according to characteristic depth levels derived from the bathymetric distribution of the North Sea, namely $z = 0$ (sea surface), 5, 10, 15, 20, 50, 60, 80, 100, 150, 200, 100, 150, 200 m. Each layer includes all mesh nodes satisfying $h \geq z$, where $h$ denotes the local water depth and $z$ the prescribed layer depth. Thus, the vertical discretization naturally adapts to spatial bathymetric variability such that shallow regions are represented by fewer active layers, whereas deeper offshore areas retain the full vertical resolution. In this manner, the approach balances computational efficiency with the need to capture vertical shear and stratification effects. Figure 1 depicts the computational meshes employed for each vertical layer, together with the sea-surface mesh used in the simulations. To ensure numerical reliability, a mesh convergence analysis was conducted. The results indicate that a mesh of 17065 elements with an area constraint of 20 km$^2$ provides an optimal compromise between accuracy and computational cost. Accordingly, this resolution is adopted throughout the present study. Bathymetric data are obtained from the GEBCO dataset and interpolated onto the generated triangular mesh using a thin-plate spline procedure, see Figure 2. This interpolation technique guarantees a smooth and consistent representation of bottom topography across elements. As a result, spurious gradients induced by discretization artifacts are

ICCS Camera Ready Version 2026
To cite this paper please use the final published version:
DOI: 10.1007/978-3-032-29924-6_3

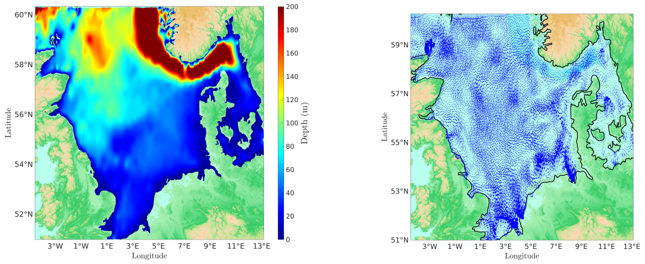

**Fig. 2.** Snapshot of the model bathymetry (left plot) used in the simulations and the corresponding sea-surface velocity field (right plot), illustrating the spatial variability of bottom topography and its dynamical influence on the surface circulation.

minimized, thereby enhancing the stability and physical fidelity of the simulated flow fields.

Once the bathymetry-conforming meshes are generated for all vertical layers, the velocity fields are computed on each layer and evaluated against observational and reanalysis products. Figure 2 presents an example of the simulated sea-surface velocity field, while Table 1 summarises the external datasets employed in the modelling framework. Surface-current validation is performed using both OSCAR and GEKCO. In particular, GEKCO is adopted as the primary reference because it combines Ekman currents at 15 m depth with surface geostrophic currents and provides daily fields, whereas OSCAR supplies 5-day averages.

Ekman currents are computed using the Ekman depth and decay constant defined in (4). For the geostrophic component, temperature and salinity fields are interpolated onto all mesh nodes across the vertical layers, and pressure, in-situ density, and specific volume anomaly are then evaluated from the thermodynamic equation of state for seawater [15]. These quantities are introduced into (7) to estimate the sub-surface geostrophic velocities. The Ekman and geostrophic components are then combined to obtain the horizontal velocity components $u$ and $v$. The vertical velocity component $w$ is derived by integrating the continuity equation (2) over the water column, with boundary conditions $w = 0$ at the sea surface ($z = 0$) and at the seabed ($z = h$), ensuring mass conservation and consistency with the theoretical framework in [19]. To represent the bottom boundary layer, the depth-averaged velocity is parameterised as one-half of the surface current magnitude. A bottom roughness length $z_0 = 0.002$ m is adopted from [18]; the friction velocity is then computed from (8) and used to construct a logarithmic near-bed velocity profile.

The initial position of each contaminant particle is prescribed within the three-dimensional computational mesh. For a particle located at $(x_p, y_p, z_p)^\top$, the nearest mesh node in the horizontal plane is first identified, and the vertical coordinate $z_p$ is then used to determine the two adjacent layers that bound the particle location. Let $d_a$ and $d_b$ denote the depths immediately above and below the particle, respectively. For each of these layers, the surrounding nodal

ICCS Camera Ready Version 2026
To cite this paper please use the final published version:
DOI: 10.1007/978-3-032-29924-6_3

**Table 1.** Overview of model data sources used in the present study, including their origin, temporal coverage, spatial resolution, and key variables analyzed.

| Source | Data set | Resolution | Increment |
|---|---|---|---|
| Natural Earth | Coastal vector data [4] | 10 miles | NA |
| SIO, UCSD | Bathymetry [3] | $(1/240)^\circ$ | NA |
| CTOH | GEKCO currents [1] | $(1/2)^\circ$ | Daily |
| NOAA | OSCAR currents [5] | $(1/3)^\circ$ | 5 days |
| NCEP | GODAS temperature [2] | $(1/3)^\circ$ | Monthly |
|  | GODAS salinity [2] | $(1/3)^\circ$ | Monthly |

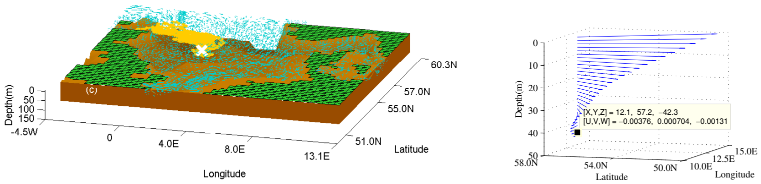

**Fig. 3.** Three-dimensional velocity field within the computational domain (left plot) and the corresponding vertical velocity profile at the contaminant release location (right plot), highlighting the local shear structure and depth-dependent flow characteristics governing initial particle transport.

velocities are averaged to obtain layer-specific estimates $\boldsymbol{v}_a$ and $\boldsymbol{v}_b$. The particle velocity is then linearly interpolated as

$$\boldsymbol{v} = f\boldsymbol{v}_b + (1-f)\boldsymbol{v}_a, \tag{12}$$

where the interpolation factor is

$$f = \frac{z_p - d_a}{d_a - d_b}. \tag{13}$$

This interpolation ensures a smooth variation of velocity with depth and avoids artificial discontinuities at layer interfaces. The same neighbouring nodes are also used to interpolate the local bathymetric depth $h$, preventing spurious particle penetration below the seabed. Repeating this procedure at each time step yields dynamically updated trajectories consistent with the evolving three-dimensional flow field. The resulting coupling between Eulerian velocities and Lagrangian particle tracking provides a stable framework for simulating contaminant transport in a stratified shelf-sea environment.

## 4 Results and discussion

In the numerical simulations, a total of 500 particles are released at the seabed from a fixed point located at latitude 57.7°N, longitude 1.01°E, and a depth of

ICCS Camera Ready Version 2026
To cite this paper please use the final published version:
DOI: 10.1007/978-3-032-29924-6_3

90 m. The temporal resolution is set to a constant time step of $\Delta t = 1$ hour; accordingly, each simulation is integrated over a period of 30 days. To account for seasonal variability, simulations are initialised at the beginning of each month for the years 2011-2013, using the corresponding hydrodynamic conditions for each period. In this way, inter-annual and intra-annual differences in circulation and stratification are systematically incorporated into the transport analysis. The released contaminant is crude oil of 40° API gravity, with a density of 825 $\mathrm{kg/m^3}$. The mean droplet diameter in seawater is estimated to lie within the range 10-100 $\mu$m [13]. Based on these characteristics, the rising velocity of the oil droplets is computed using (11), yielding physically realistic ascent speeds between 0.01 and 0.1 m/s. Consequently, buoyancy-driven vertical transport competes with advective and shear-induced dispersion during the early stages following release. The source location corresponds to the Forties Oil Field in the North Sea, while the designated risk area extends from 56.7°N to 58.7°N and from 2.0°E to 2.5°E. Figure 3 presents the three-dimensional flow structure together with the vertical velocity profile at the release site. Under the simulated conditions, the relative geostrophic component is found to be weak; therefore, the circulation exhibits predominantly barotropic characteristics, with geostrophic velocities displaying minimal depth dependence. An examination of hydrographic data for the period 2011-2013 indicates that salinity varies between 33 and 35 ppt, whereas temperature ranges from 6°C to 17°C. As a result, seawater density remains approximately constant at about 1027 $\mathrm{kg/m^3}$, leading to a small geopotential height gradient across the domain. This limited density contrast further explains the subdued baroclinic contribution to the geostrophic flow. Boundary layer diagnostics reveal that the bottom boundary layer thickness is approximately one-third of the total water depth $h$. For representative depths of 40 m and surface current velocities between 0.05 and 0.15 m/s, the associated friction velocity ranges from 0.01 to 0.05 m/s, corresponding to a boundary layer thickness of roughly 15 m. This estimate lies well within the commonly reported range of 5-60 m for large-scale ocean circulation [22], thereby supporting the physical consistency of the parameterization. Furthermore, the Ekman layer depths computed from (4) vary between 40 and 70 m. During summer months, enhanced wind variability tends to produce a shallower Ekman layer, typically around 40 m. In addition, the decay constant $a$ assumes values between 0.03 and 0.05, implying an integrated current rotation of approximately 70°-90° across the water column. Taken together, these dynamical characteristics delineate a circulation regime in which wind-driven processes dominate vertical structure, while density-driven effects remain comparatively weak.

To assess model performance, the simulated flow fields are systematically compared with independent datasets, namely GEKCO, OSCAR, and available moored current meter observations. Through this multi-source validation strategy, both large-scale circulation patterns and local velocity structures are evaluated. In parallel, the error associated with the dispersion model (9) is quantified by decomposing it into two principal components namely, the advective error arising from uncertainties in the current field and the parameterised dispersion

ICCS Camera Ready Version 2026
To cite this paper please use the final published version:
DOI: 10.1007/978-3-032-29924-6_3

error. This separation enables a clearer interpretation of the respective contributions of resolved flow dynamics and subgrid-scale mixing processes. The statistical agreement between model results and reference datasets is evaluated using the Willmott Index of Agreement (WS) [23], defined as

$$\mathrm{WS} = 1 - \frac{\sum_{i=1}^{72} \left(U_{G,i} - U_i\right)^2}{\sum_{i=1}^{72} \left(\left|U_{G,i} - \overline{U}\right| + \left|U_i - \overline{U}\right|\right)^2}, \tag{14}$$

where $U$ denotes the simulated velocity magnitude (m/s) or direction (°), $U_G$ represents the corresponding GEKCO reference values, and $\overline{U}$ is the annual mean of the simulated velocity magnitude or direction. The summation extends from $i = 1$ to 72, reflecting the 5-day averaged temporal resolution provided by GEKCO, which yields 72 data points per year. The index ranges between 0 and 1, with $\mathrm{WS} = 1$ indicating perfect agreement and $\mathrm{WS} = 0$ denoting the absence of predictive skill. In the present simulations, WS values of 0.41 for velocity magnitude and 0.52 for velocity direction are obtained when compared with GEKCO and OSCAR datasets. These values indicate moderate agreement, particularly in directional representation, while highlighting residual discrepancies in current intensity. Furthermore, the reliability of the reference datasets themselves is considered. It is worth noting that GEKCO and OSCAR have both been independently validated against moored current meters and surface drifters. Reported correlations are approximately $0.7 \pm 0.1$ for GEKCO [21] and $0.5 \pm 0.1$ for OSCAR [12]. Hence, GEKCO demonstrates comparatively stronger agreement with in-situ observations. This finding is consistent with previous analyses [12], which indicate that OSCAR amplitude predictions tend to degrade at latitudes exceeding 10°. In light of these validation statistics, the advective error in the present model is conservatively estimated at approximately 30%, based on the reported GEKCO correlation with surface drifters. Accordingly, this value is adopted as a representative uncertainty bound for the resolved current field. Through this layered validation approach, combining statistical skill assessment, cross-dataset comparison, and reference-data evaluation, the robustness and limitations of the simulated flow and dispersion fields are quantitatively established.

Figure 4 presents the velocity fields and corresponding particle trajectories at selected days following release for December 2011 and June 2013, thereby highlighting the pronounced seasonal variability in transport pathways and dispersion patterns. For clarity of presentation, only a localized subregion of the computational domain surrounding the release site is displayed; nevertheless, the depicted dynamics remain representative of the broader circulation regime. The horizontal dispersion coefficients $D_{xx}$ and $D_{yy}$ are evaluated for representative current magnitudes of 0.05-0.15 m/s at depths of 50 m and 100 m. At 50 m depth, the resulting values are $D_{xx} = 3 \times 10^3$ cm$^2$/s and $D_{yy} = 2 \times 10^4$ cm$^2$/s. At 100 m depth, the coefficients increase to $D_{xx} = 5 \times 10^3$ cm$^2$/s and $D_{yy} = 3 \times 10^4$ cm$^2$/s. These magnitudes are consistent with classical estimates of

ICCS Camera Ready Version 2026
To cite this paper please use the final published version:
DOI: 10.1007/978-3-032-29924-6_3

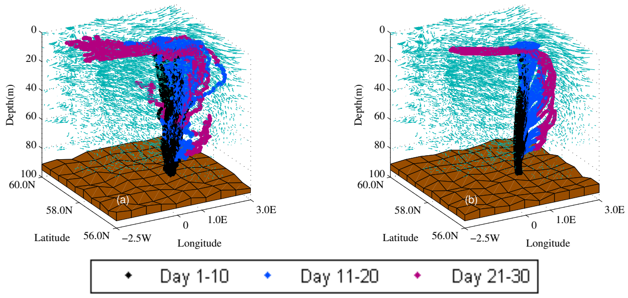

**Fig. 4.** Velocity fields and corresponding particle trajectories at selected days following release for December 2011 (left plot) and June 2013 (right plot), illustrating the seasonal variability in transport pathways and dispersion patterns. For improved visual clarity, only a localized subregion of the computational domain surrounding the release site is shown.

mixing coefficients reported in the literature. However, whereas classical parameterizations predict a decrease in mixing intensity with height above the seabed, the present estimates exhibit a moderate increase with depth. This difference reflects the local shear structure and wind-driven variability characteristic of the North Sea during the considered period. The simulated contaminant distributions after 30 days demonstrate a strong dependence on the month of release. In particular, particles advect with mean speeds of approximately 0.2 m/s during summer months and 0.26 m/s during winter months, indicating enhanced transport under stronger winter circulation. For a given release month, the ratio of advective to dispersive transport rates, corresponding to the second and third terms in (9), is approximately 0.4. Thus, although advection governs large-scale displacement, dispersion contributes substantially to the spatial spreading of the contaminant plume. Because the dispersive term in (9) is stochastic, each simulation is repeated 1000 times as part of a Monte Carlo uncertainty analysis. The ensemble mean particle position is computed for each month, and the deviation of individual realisations from this mean is quantified. The standard error associated with stochastic dispersion is estimated as $\sigma/N$, expressed as a percentage of the ensemble mean, where $\sigma$ denotes the standard deviation and $N = 1000$ the number of realisations. The resulting percentage uncertainty due to dispersive variability is approximately 5% across all particles and release months, thereby indicating robust ensemble convergence. To estimate the total model uncertainty, advective and dispersive errors are subsequently combined. Assuming that an average particle travels approximately 750 km over the simulation period and adopting a representative dispersion-advection ratio of 0.4, the displacement attributable to advection and dispersion is approximately 300 km and 450 km, respectively. Incorporating the estimated uncertainties yields distances of $300 \pm 60$ km for advection and $450 \pm 10$ km for dispersion, leading to a combined displacement of $750 \pm 90$ km. Consequently, the aggregate model

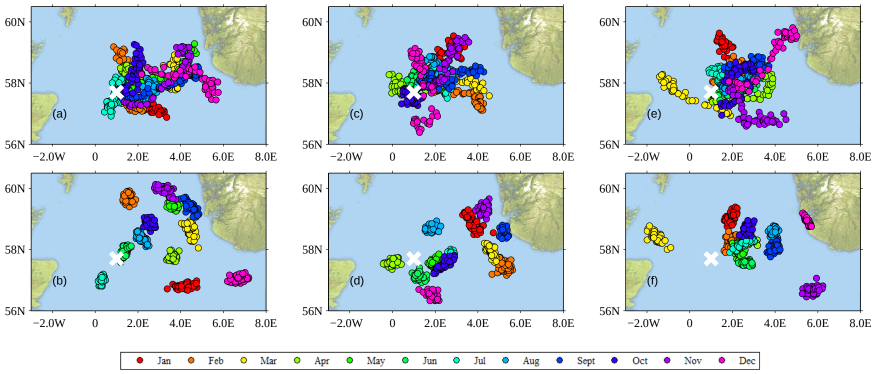

**Fig. 5.** Spatial distributions of contaminant particles for each monthly release illustrating the seasonal variability in transport pathways, surface spreading, and shoreline exposure risk. Here, each plot corresponds to a separate release month and shows particle positions after the 30-day simulation period, thereby enabling a comparative assessment of the influence of changing hydrodynamic conditions on dispersion patterns for 2011 (a), 2012 (c) and 2013 (e) in two-dimensional releases and 2011 (b), 2012 (d) and 2013 (f) in three-dimensional releases.

uncertainty is approximately 17%. This quantitative error assessment provides a transparent measure of predictive reliability and strengthens confidence in the simulated transport patterns under the considered seasonal conditions.

A detailed depiction of particle distributions for each monthly release during 2012 is presented in Figure 5. These results reveal a pronounced seasonal dependence in transport pathways. In most cases, particles drift eastward following release; however, the April simulation exhibits a marked westward displacement. Consequently, this scenario suggests a temporary shift in circulation patterns that could pose a potential threat to the Norwegian coastline within approximately one to three months after release. During the April experiment, the oil droplets with the highest prescribed rising velocity (0.1 m/s) reach the sea surface in just under 10 days. This ascent time is longer than anticipated and likely reflects a scaling inconsistency in the vertical velocity parameterization. Ideally, the rise time should range from several hours to a few days, consistent with field observations reported in [13]. Nevertheless, once the oil droplets reach the surface, horizontal advection by surface currents becomes increasingly dominant, as evidenced by the enhanced lateral spreading visible in Figure 5. The ensemble-averaged trajectories further illustrate the distinction between purely advective transport and combined advective-dispersive motion. In general, wind-driven (Ekman) currents exhibit greater temporal variability than geostrophic currents, particularly during summer months, with magnitudes fluctuating between 0 and 0.1 m/s. By contrast, the geostrophic component, linked to sea-surface height gradients influenced in part by tidal dynamics, displays a comparatively stable and predictable structure. However, because the considered wind magnitude and

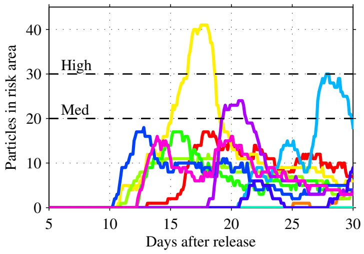

**Fig. 6.** Temporal evolution of the number of particles entering the defined risk area for each monthly release scenario. The curves illustrate the cumulative particle count within the specified geographic bounds over the 30-day simulation period, thereby quantifying the relative exposure under varying seasonal circulation conditions. Here, the legend and corresponding colour scheme are consistent with those presented in Figure 5.

direction frequently dominate the total surface flow, the net transport of contaminants is typically directed eastward. The prevailing eastward drift observed in Figure 5 can be attributed to anomalies in both the magnitude and direction of the surface current components. Specifically, GEKCO data indicate a substantial increase in geostrophic current magnitude during mid-to-late April 2012, rising from approximately 0.07 m/s to 0.23 m/s. Simultaneously, the Ekman component maintains speeds near 0.1 m/s. Importantly, the directions of both components during much of April exhibit an east-to-west orientation, thereby favouring westward contaminant transport and explaining the April outcome. Such a reversal in flow direction appears to be relatively uncommon within the analysed period. Indeed, only one out of the 36 monthly simulations (three years, twelve releases per year) resulted in westward transport posing a potential risk to the United Kingdom, corresponding to approximately 3% of cases. Therefore, although episodic circulation anomalies may temporarily alter transport pathways, the statistical likelihood of significant westward contaminant drift from the Forties Oil Field toward the UK coastline remains low under the examined hydrodynamic conditions.

For the risk assessment, the number of particles entering the predefined risk area is quantified for each monthly release during 2012, as presented in Figure 6. This metric provides a direct measure of potential shoreline exposure under varying seasonal circulation regimes. The results indicate that contaminant particles do not enter the risk area immediately after release; rather, they typically arrive approximately 10 days post-release, having travelled a distance of roughly 200 km. This delay reflects the combined effects of horizontal advection, vertical ascent, and lateral dispersion. Consequently, short-term coastal exposure within the first week following a release appears unlikely under the simulated hydrodynamic conditions. The predefined medium-risk threshold of 20 particles is exceeded during July and November, whereas the high-risk threshold of 30

ICCS Camera Ready Version 2026
To cite this paper please use the final published version:
DOI: 10.1007/978-3-032-29924-6_3

particles is surpassed in April. These exceedances underscore the importance of seasonal variability in circulation patterns, as changes in wind forcing and current structure substantially alter transport pathways and accumulation rates within the risk zone. Furthermore, particles characterised by slower rising velocities remain within the risk area for extended durations. In some cases, approximately 10% of the released particles persist within the defined bounds at the final of the 30-day simulation period. This prolonged residence time increases the potential for sustained environmental exposure, particularly when combined with recurrent or episodic releases. Taken together, these findings demonstrate that both the timing of release and the vertical ascent characteristics of the contaminant critically influence coastal risk levels. Accordingly, accurate representation of seasonal hydrodynamics and buoyancy-driven processes is essential for reliable impact forecasting in offshore spill scenarios.

Finally, an analysis of the computational cost associated with a single 30-day simulation involving 1000 particles indicates that the dominant contribution to total CPU time arises from the computation of the hydrodynamic velocity field. This component includes the solution of the multilayer flow equations and the associated interpolation procedures required to provide velocity inputs for particle tracking. Consequently, the Eulerian flow solver constitutes the principal computational bottleneck of the modelling method. In contrast, the numerical integration of the stochastic advection-dispersion equations governing particle motion accounts for approximately 24% of the total CPU time. Although the Lagrangian particle-tracking component involves repeated evaluation of interpolated velocities and random dispersive increments, its computational demand remains secondary to that of the flow-field simulation. An additional 6% of the total computational time is primarily devoted to post-processing tasks, including particle counting within the risk area and graphical output generation. Therefore, only a relatively small fraction of resources is allocated to analysis and visualisation compared with the core hydrodynamic computations. Because the simulation horizon is fixed at 30 days for all scenarios, the total runtime remains largely unchanged across experiments. Accordingly, variations in computational cost are influenced more strongly by the complexity of the velocity field calculations than by differences in release month or particle behaviour. This performance assessment demonstrates that the proposed modelling method achieves a balanced compromise between physical fidelity and computational efficiency, rendering it suitable for repeated ensemble simulations and uncertainty quantification studies.

## 5 Conclusions

This study developed an advanced computational model to simulate pollution dispersion in the North Sea by integrating physics-based hydrodynamic modelling with observational data for currents and bathymetry. Oceanographic equations of motion were applied to estimate sub-surface currents, with vertical structure represented through a turbulent boundary layer parameterization. The re-

ICCS Camera Ready Version 2026
To cite this paper please use the final published version:
DOI: 10.1007/978-3-032-29924-6_3

sulting velocity fields were subsequently coupled to an advective-dispersive random walk model, enabling probabilistic prediction of contaminant transport and quantification of shoreline impact risk following a hypothetical release from the Forties Oil Field. The simulations indicate that the probability of contaminant landfall along the UK coastline is low, approximately 3%, with the overwhelming majority of simulated releases advected eastward toward the Norwegian coast. This dominant eastward transport is primarily driven by prevailing wind forcing. On average, particles travelled approximately 600 km over a 30-day period and seasonal variability was found to exert a significant influence on dispersion characteristics, with higher particle velocities and enhanced transport observed during winter months. Model performance was encouraging, with error estimates on the order of 17%. Nevertheless, several sources of uncertainty remain, particularly in the estimation of dispersion coefficients and in the representation of complex current structures. The principal opportunity for model enhancement lies in refining the hydrodynamic component of the method. Future work will focus on implementing a baroclinic modelling approach using the Hamburg Shelf Ocean Model (HAMSOM). Coupling this methodology with the North-West European Shelf (NWES) system would improve boundary condition representation and enable explicit treatment of volume fluxes entering and leaving the computational domain. Such an approach would allow externally driven currents, including the Shetland Current, to be incorporated more realistically into circulation estimates. Atmospheric forcing and sea-surface topography datasets (e.g., GEKCO) would provide input to HAMSOM, replacing daily current fields while preserving the particle-tracking simulation and post-processing methodology developed in this study. In summary, this work demonstrates the feasibility of combining deterministic hydrodynamic modelling with stochastic dispersion techniques to produce robust, risk-based assessments of offshore contaminant transport. Based on improved circulation modelling and boundary coupling, the method has strong potential to evolve into a comprehensive predictive tool for environmental risk management in the North Sea.

## 6 Acknowledgments

We would like to thank the Moroccan Ministry of Higher Education, Scientific Research and Innovation and the OCP Foundation who funded this work through the APRD research program.

## References

1. Geostrophic and ekman current observatory (gekco). http://www.legos.obs-mip.fr, accessed: 2026
2. Global ocean data assimilation system (godas). http://www.esrl.noaa.gov/psd/data/gridded/data.godas.html, accessed: 2026
3. Global topography tool (sio, ucsd). http://topex.ucsd.edu, accessed: 2026
4. Natural earth coastline vector data. http://www.naturalearthdata.com, accessed: 2026

ICCS Camera Ready Version 2026
To cite this paper please use the final published version:
DOI: 10.1007/978-3-032-29924-6_3

5. Ocean surface current analyses real-time (oscar). http://www.oscar.noaa.gov, accessed: 2026
6. Anzani, H.S., Kantoush, S.A., Kobayashi, S.: Impact of bed roughness configurations on flow dynamics and hydraulic resistance in open-channel flows. Scientific Reports **16**, 3614 (2025)
7. Beyer, J., Ellingsen, K.E., Yoccoz, N.G., Buhl-Mortensen, P., Bakke, T.: Environmental effects monitoring of offshore oil and gas activities on the norwegian continental shelf: A review. Marine Environmental Research **209**, 107166 (2025)
8. Carpenter, A.: Oil pollution in the north sea: the impact of governance measures on oil pollution over several decades. Hydrobiologia **845**, 109–127 (2019)
9. De Serio, F., Mossa, M.: Streamwise velocity profiles in coastal currents. Environmental Fluid Mechanics **14**(4), 895–918 (2014)
10. El-Amrani, M., Seaid, M.: An essentially non-oscillatory semi-lagrangian method for tidal flow simulations. International Journal for Numerical Methods in Engineering **81**(7), 805–834 (2010)
11. Falconer, R.A., Ismail, A.I.B.M.: Numerical modelling of tracer transport in a contact tank. Environment International **23**(6), 763–773 (1997)
12. Johnson, E.S., Bonjean, F., Lagerloef, G.S.E., Gunn, J.T., Mitchum, G.T.: Validation and error analysis of oscar sea surface currents. Journal of Atmospheric and Oceanic Technology **24**, 688–701 (2007)
13. Keramea, P., Spanoudaki, K., Zodiatis, G., Gikas, G., Sylaios, G.: Oil spill modeling: A critical review on current trends, perspectives, and challenges. Journal of Marine Science and Engineering **9**(2), 181 (2021)
14. Kitanidis, P.K.: Particle tracking equations for the solution of the advection-dispersion equation with variable coefficients. Water Resources Research **30**(11), 3225–3227 (1994)
15. Millero, F.J., Huang, F.: The density of seawater as a function of salinity and temperature. Ocean Science **5**, 91–100 (2009)
16. Sari, S., Rowan, T., Seaid, M., Benkhaldoun, F.: Simulation of three-dimensional free-surface flows using two-dimensional multilayer shallow water equations. Communications in Computational Physics **27**(5), 1413–1442 (2020)
17. Skognes, K., Johansen, O.: Statmap: a 3-dimensional model for oil spill risk assessment. Environmental Modelling and Software **19**, 727–737 (2004)
18. Stanev, E.V., Dobrynin, M., Pleskachevsky, A., Grayek, S., Gunther, H.: Bed shear stress in the southern north sea as an important driver for suspended sediment dynamics. Ocean Dynamics **59**, 183–194 (2008)
19. Stewart, R.H.: Introduction to Physical Oceanography. Texas A&M University (2005)
20. Sudre, J., Maes, C., Garçon, V.: On the global estimates of geostrophic and ekman surface currents. Limnology and Oceanography: Fluids and Environments **3**, 1–20 (2013)
21. Sudre, J., Morrow, R.A.: Global surface currents: a high-resolution product for investigating ocean dynamics. Ocean Dynamics **58**, 101–118 (2008)
22. Trowbridge, J.H., Lentz, S.J.: The bottom boundary layer. Annual Review of Marine Science **10**, 397–420 (2018)
23. Willmott, C.J., Robeson, S.M., Matsuura, K.: A refined index of model performance. International Journal of Climatology **32**(13), 2088–2094 (2012)

ICCS Camera Ready Version 2026
To cite this paper please use the final published version:
DOI: 10.1007/978-3-032-29924-6_3